nature communications

Article

https://doi.org/10.1038/s41467-024-53927-6

Room-temperature selective cyclodehydrogenation on Au(111) via radical addition of open-shell resonance structures

Received: 10 April 2024

Accepted: 25 October 2024

Published online: 05 November 2024

Check for updates

Deng-Yuan Li[1] ✉, Zheng-Yang Huang[2], Li-Xia Kang[2], Bing-Xin Wang[2], Jian-Hui Fu[2], Ying Wang[2], Guang-Yan Xing[2], Yan Zhao[2], Xin-Yu Zhang[2] & Pei-Nian Liu[1,2] ✉

Cyclodehydrogenation is an important ring-formation reaction that can directly produce planar-conjugated carbon-based nanomaterials from nonplanar molecules. However, inherently high C–H bond energy necessitates a high temperature during dehydrogenation, and the ubiquity of C − H bonds in molecules and small differences in their bond energies hinder the selectivity of dehydrogenation. Here, we report a room-temperature cyclodehydrogenation reaction on Au(111) via radical addition of open-shell resonance structures and demonstrate that radical addition significantly decreases cyclodehydrogenation temperature and further improves the chemoselectivity of dehydrogenation. Using scanning tunneling microscopy and non-contact atomic force microscopy, we visualize the cascade reaction process involved in cyclodehydrogenation and determine atomic structures and molecular orbitals of the planar acetylene-linked oxa-nanographene products. The nonplanar intermediates observed during progression annealing, combined with density functional theory calculations, suggest that room-temperature cyclodehydrogenation involves the formation of transient radicals, intramolecular radical addition, and hydrogen elimination; and that the high chemoselectivity of cyclodehydrogenation arises from the reversibility and different thermodynamics of radical addition step.

Dehydrogenation, an important chemical transformation involving the removal of one or more hydrogen atoms, has broad synthetic utility[1–4]. For example, dehydrogenation is a fundamental chemical process in the petrochemical industry for transforming low-value alkanes into high-value-added chemicals[2,3]. The intramolecular dehydrogenation coupling reaction in solution chemistry is one of the key steps for achieving planarization and aromatization of molecules to synthesize functional large π-conjugated systems[1,4]. Over the past 15 years, dehydrogenation reactions on surfaces under ultrahigh-vacuum (UHV) conditions have been developed and visualized by scanning probe microscopy[5–10], providing valuable experimental insights for selective C–H bond activation[11–14], surface/adatom catalytic mechanism[14–17], and covalent polymerization at the molecular level[18–20]. Particularly, intramolecular cyclodehydrogenation[18], as a key step in achieving planarization and aromatization from nonplanar molecules or reaction intermediates on surfaces, has been frequently used to fabricate various low-dimensional covalent carbon-based nanostructures[21–30], such as nanographenes[18,30–36], graphene nanoribbons[37–42], and other carbon allotropes[43], whose synthesis can be challenging through conventional solution chemistry. However, cyclodehydrogenation reactions usually

[1]State Key Laboratory of Natural Medicines, School of Pharmacy, China Pharmaceutical University, 211198 Nanjing, P. R. China. [2]School of Chemistry and Molecular Engineering, East China University of Science & Technology, 200237 Shanghai, P. R. China. ✉e-mail: dengyuanli@cpu.edu.cn; liupn@ecust.edu.cn

require harsh conditions (high temperature, approximately 573 K on the Au(111) surface) owing to the inherently high C − H bond energy. The ubiquity of C − H bonds in molecules and the small difference in bond energy also hamper the selectivity of the dehydrogenation reactions. Therefore, realizing highly selective cyclodehydrogenation on surfaces under mild conditions is desirable, although it remains a great challenge.

Free radicals are highly chemically reactive species with at least one unpaired valence electron and are key intermediates in many chemical transformations[44–48]. Generally, free radicals on surfaces (Fig. 1a) are generated by homolyzing covalent *σ*-bonds (such as carbon–halogen bonds)[49,50] or π-bonds (intramolecular electrocyclization of unsaturated groups)[51–54]. However, the free radicals on surfaces are easily quenched by metal surfaces or adatoms, generating more stable organometallic intermediates[50,55–59]. The highly active free radicals also tend to self-passivate to form new covalent bonds[57,60,61]. These radical quenching effects hinder the application in controlling on-surface covalent reactions. Another possible route for forming free radicals is molecular resonance (Fig. 1b), which may generate transient radicals and avoid the quenching effects because the energy difference between the closed-shell and open-shell resonance hybrid structures is small[62–64]. As a typical example, Fasel et al. reported a lateral fusion of open-shell indeno[2,1-b]fluorene polymers on Au(111) at approximately 573 K to form porous ribbons[62]. In contrast, room-temperature cyclodehydrogenation on Au(111) remains underexplored and the selectivity of dehydrogenation needs to be improved.

In this work, we report a room-temperature cyclodehydrogenation reaction with high chemoselectivity on Au(111) via radical addition of open-shell resonance structures and demonstrate that radical addition can significantly decrease the temperature of cyclodehydrogenation. Through debromination coupling of *gem*-dibromides, cumulene-containing nonplanar coupling products are first produced on Au(111) and can generate transient radicals via resonance from cumulene to internal alkyne. The subsequent intramolecular radical addition gives nonplanar cyclized intermediates that easily undergo dehydrogenation to attain planarization and aromatization, affording planar acetylene-linked oxa-nanographene products (Fig. 1c). The atomic structures and molecular orbitals of oxa-nanographenes are determined by a combination of scanning tunneling microscopy/spectroscopy (STM/STS), bond-resolved STM (BR-STM), non-contact atomic force microscopy (nc-AFM), and density functional theory (DFT) calculations. The diverse nonplanar intermediates, along with the DFT calculation results demonstrated that room-temperature cyclodehydrogenation involved the formation of transient radicals, intramolecular radical addition, and hydrogen elimination; and that the high chemoselectivity of the cyclodehydrogenation arises from the reversibility and different thermodynamics of the radical addition step.

Results

Initially, 10-(dibromomethylene)-[1,2′-bianthracen]−9(10*H*)-one (**1**) was selected as a model precursor for the in situ formation of cumulenic dimer on the Au(111) surface through selective debrominative C–C coupling reaction of *gem*-dibromides[65,66]. This dimer is expected to be an ideal active intermediate for the generation of transient radicals via resonance from cumulene to internal alkyne on Au(111) (Fig. 1c and Supplementary Fig. 1). Moreover, the radical shift from C to O through resonance from cyclohexadienone radical to the phenoxyl radical (similar to the keto-enol tautomerism) and intramolecular radical addition with the adjacent phenyl group give a nonplanar radical intermediate. As a result, the nonplanar radical intermediate may easily undergo dehydrogenation to attain planarization and aromatization, affording planar acetylene-linked oxa-nanographene products (Fig. 1c).

After depositing precursor **1** on the Au(111) surface held at room temperature (approximately 300 K) for 12 h under UHV conditions, the

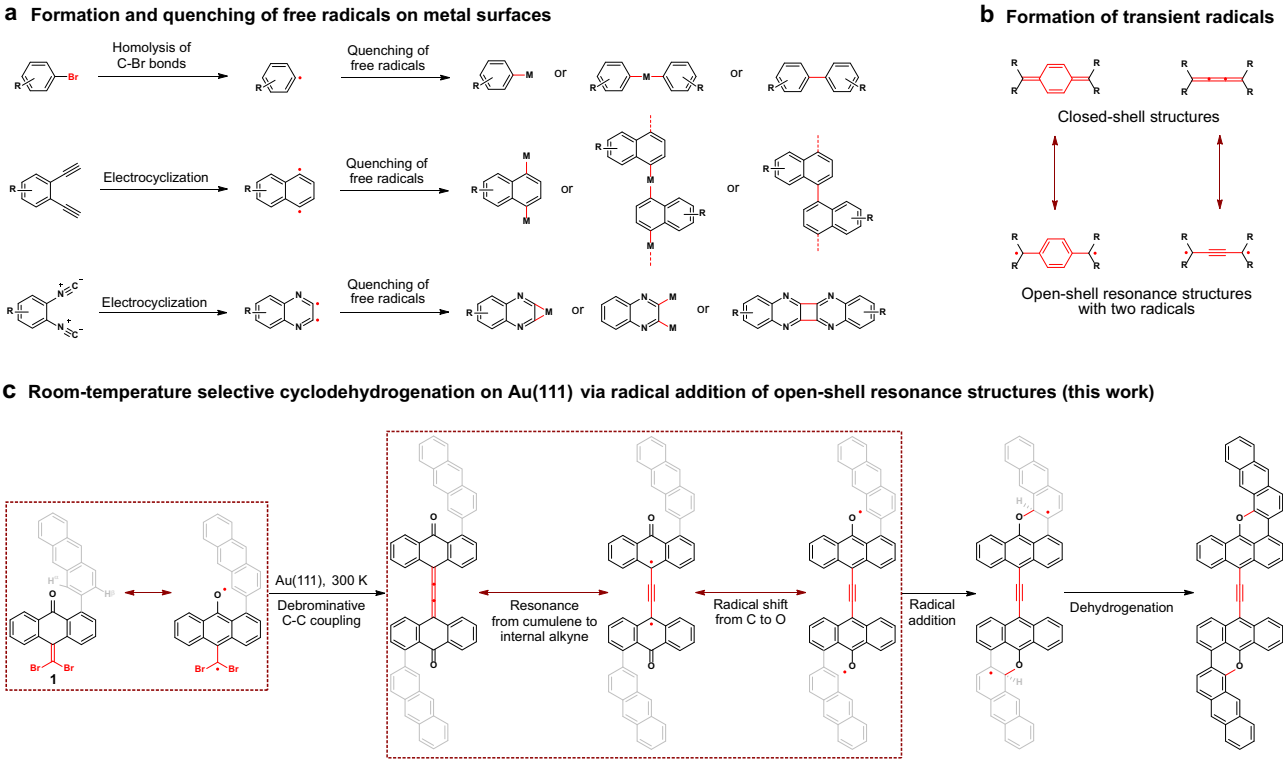

Fig. 1 | Strategy for inducing room-temperature cyclodehydrogenation on Au(111). a Formation and quenching of free radicals on metal surfaces ("M" indicates the metal adatom or metal surface. "R" indicates the substituent groups). **b** Formation of transient radicals. **c** Inducing room-temperature cyclodehydrogenation on Au(111) via radical addition of open-shell resonance structures (The gray chemical structure represents the part of the molecule closer to the Au(111) surface).

https://doi.org/10.1038/s41467-024-53927-6

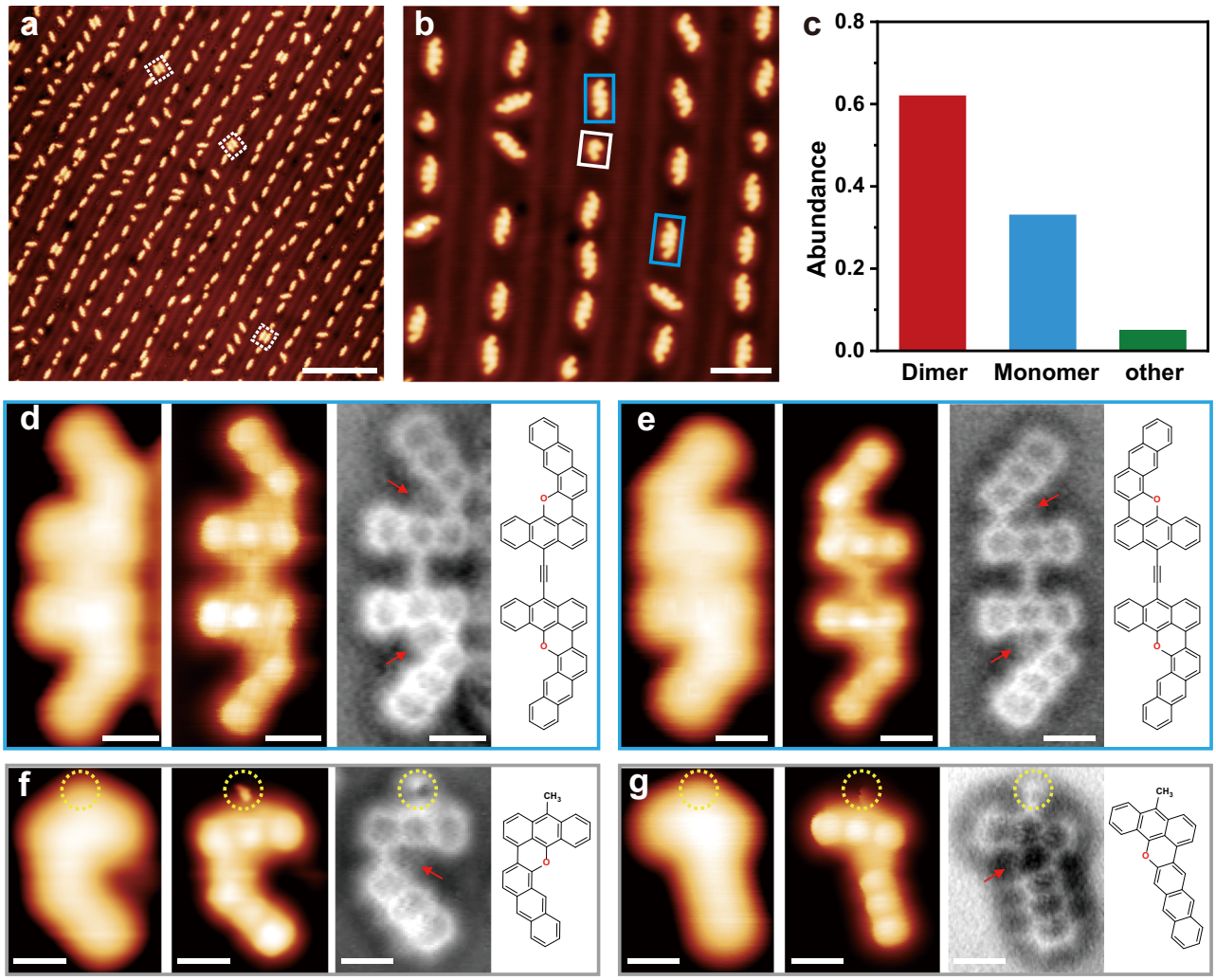

Fig. 2 | Formation and structural characterization of planar oxa-nanographenes on Au(111) via room-temperature cyclodehydrogenation. **a**–**c** Large-scale and high-resolution STM images after depositing precursor **1** on Au(111) held at 300 K for 12 h and the corresponding statistical analysis of products. **d, e** Zoom-in STM, BR-STM, and nc-AFM images of two representative planar dimers formed by the removal of *α*-H and the corresponding chemical structures. **f**, **g** Zoom-in STM, BR-STM, and nc-AFM images of two representative planar monomers (**f**: *cis*-monomer; **g**: *trans*-monomer) and the corresponding chemical structures. The red arrows and yellow dotted circles indicate O atoms and methyl groups. Scale bars: **a** 20 nm. **b** 5 nm. **d**–**g** 0.5 nm. Scanning parameters: **a** $U = 0.5$ V, $I = 10$ pA. **b** $U = 0.2$ V, $I = 50$ pA. **d,e** $U = 0.1$ V, $I = 100$ pA. **f** $U = 0.1$ V, $I = 10$ pA. **g** $U = 0.2$ V, $I = 8$ pA. **d**-**g** BR-STM: CO tip, constant height, $U = 10$ mV.

sample was cooled to approximately 5 K for further characterization. Large-scale STM images reveal the formation of diverse individual dimers and monomers that are adsorbed on the face-centered cubic regions of Au(111) surfaces herringbone reconstruction aligning with [11-2] and the equivalent direction of the substrate (Fig. 2a and Supplementary Fig. 2). The high-resolution STM image reveals two frequently observed species, including two types of dimers (blue frames in Fig. 2b) and one typical *cis*-monomer (gray frame in Fig. 2b). As shown in zoom-in STM images, one dimer has a mirror-symmetric structure (Fig. 2d, left) and the other dimer has a centrosymmetric structure (Fig. 2e, left). Further, BR-STM and nc-AFM images reveal that the two dimers have planar geometries with their termini present in a *cis*-configuration. These structural features suggest that the two planar dimers are the desired acetylene-linked oxa-nanographene products (Supplementary Fig. 3a, b). Notably, only a few bromide atoms are observed between two planar *cis*-α,α-dimers (while dotted frames in Fig. 2a and Supplementary Fig. 4). These results further demonstrate that precursor **1** undergoes debrominative C–C coupling and intramolecular cyclodehydrogenation by the removal of *α*-H on Au(111) at room temperature.

Similarly, the zoom-in STM, BR-STM, and nc-AFM images (Fig. 2f and Supplementary Figs. 3c and 5) of a common *cis*-monomer product indicate a planar geometry with a bright protrusion at the terminal (yellow dotted circles in Fig. 2f), and this bright protrusion can be assigned to a methyl group (CH_3)[67,68]. Moreover, the *trans*-monomer product is occasionally observed in the experimental STM images, and the chemical structure is identified from corresponding zoom-in STM, BR-STM, and nc-AFM images (Fig. 2g and Supplementary Fig. 3d). The results suggest that the debromination process is possibly accompanied by hydrogen passivation by the active hydrogen adatoms (formed by the molecular hydrogen cracked by the filament in the residual gas of the UHV chamber). Statistical analysis based on the counting of the number of planar versus nonplanar species on the Au(111) surface reveals that planar dimers and monomers account for approximately 95%, corresponding to 62% dimers (more than 61% *α*,*α*-dimers and less than 1% *α*,*β*- and *β*,*β*-dimers) and 33% monomers (Fig. 2c). The selectivity of the *α*-site cyclodehydrogention is up to 99% and only a few *β*-site cyclodehydrogenation products can be observed, suggesting that room-temperature intramolecular cyclodehydrogenation is a highly chemoselective reaction.

After further annealing at 333 K for 15 minutes, most planar dimer and monomer products remain intact with the same statistical abundance as at room temperature (Supplementary Fig. 6a, b). STM images show that when the sample was annealed at 543 K for 15 min, most planar dimers were still intact with only a few containing deformed kinks in the middle of the molecular backbone (Supplementary Fig. 6c), which may be attributed to the high temperature-induced intramolecular cyclization of the alkyne groups with two adjacent anthracene moieties[69]. In contrast, the planar monomer products are significantly less than that at room temperature or 333 K, which can be attributed to the high temperature-induced desorption of smaller monomers from Au(111). The chemical structures of the other configurational dimers are also determined from the zoom-in STM and BR-STM images (Supplementary Fig. 7).

To demonstrate the radical addition-induced room-temperature cyclodehydrogenation of precursor **1** on Au(111), we performed a control experiment using [1,2′-bianthracene]−9,10-dione (AAQ), which does not contain dibromomethylene (CBr_2) group, as a precursor. The STM images obtained after dosing Au(111) with AAQ by exposing the latter to the evaluated temperature show that no obvious planar species are formed at room temperature even after annealing to 333 K and that only dimers comprising the self-assembly of two nonplanar AAQ molecules are dispersedly adsorbed on the Au(111) surface (Supplementary Fig. 8a, b); this is further supported by bias-dependent STM images (Supplementary Fig. 8c) and the corresponding simulation based on DFT-optimized structure model (Supplementary Fig. 8d). These results further demonstrate that radical addition significantly decreases the temperature of intramolecular cylodehydrogenation on Au(111).

Next, differential conductance spectroscopy (dI/dV) was performed to characterize the electronic structures of the planar acetylene-linked oxa-nanographenes (Fig. 3). The dI/dV spectra of three representative acetylene-linked oxa-nanographenes on Au(111) show two typical resonance states at approximately −0.5 and 1.8 V for the *α,α*-dimer (Fig. 3a), −0.6 and 1.6 V for the *β,β*-dimer (Fig. 3c), and −0.5 and 1.6 V for the α,β-dimer (Fig. 3e). The constant-current dI/dV maps reveal that three oxa-nanographenes exist in a similar state at negative voltages and are mainly distributed in two middle anthracenes connecting the alkynyl group, and the states at positive voltages are slightly different and located at the armchair edge of the two middle and terminal anthracenes (Fig. 3b, d, f). These features further resemble the local density of states maps of the HOMO and mixed LUMO containing LUMO and LUMO + 1 (Fig. 3 and Supplementary Fig. 9), demonstrating that the two states at the negative and positive

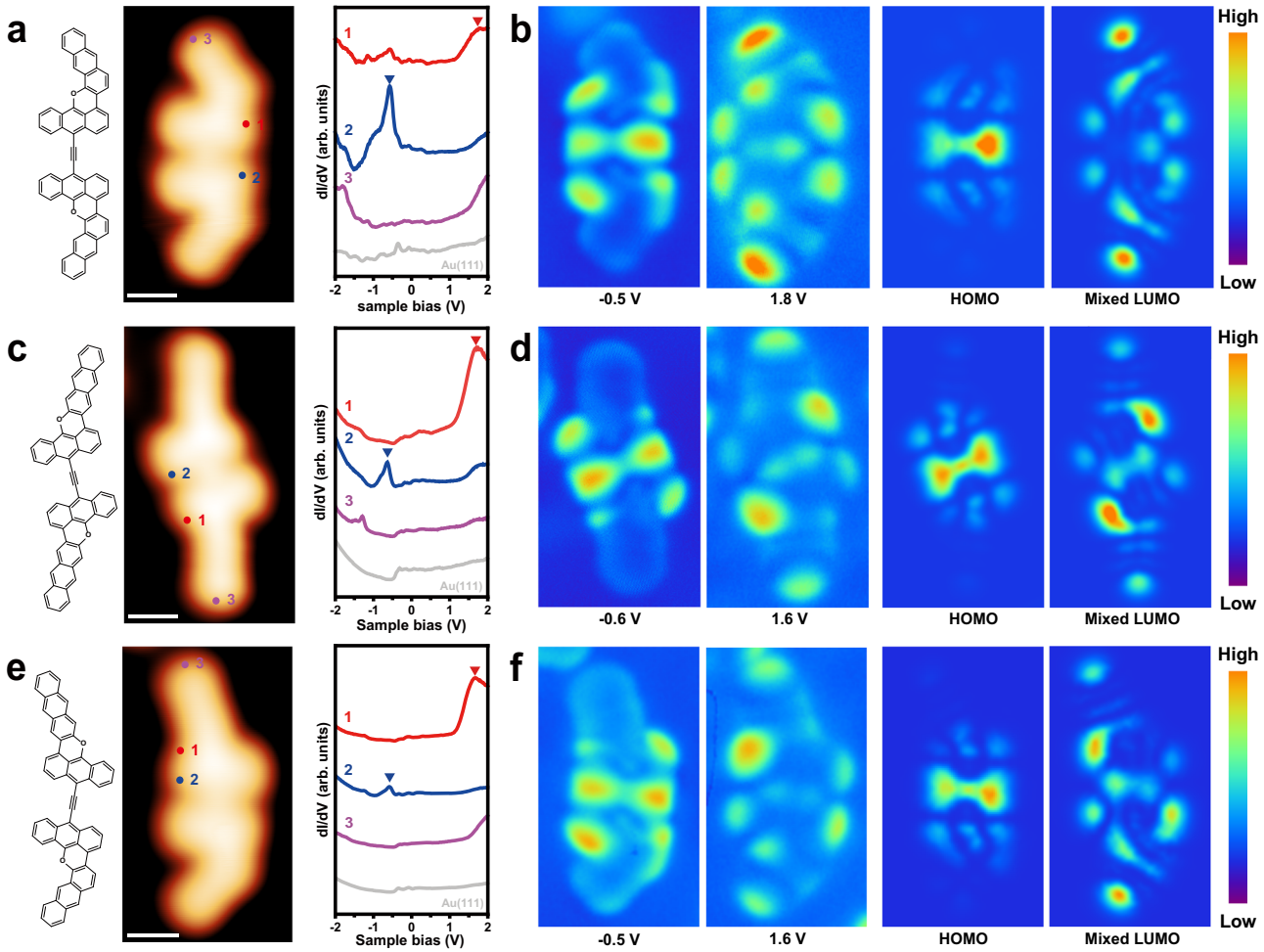

Fig. 3 | Electronic properties of three representative planar acetylene-linked oxa-nanographenes on Au(111). a, **c, e** Chemical structures, STM images, and dI/dV spectra recorded on different locations (marked in the inset STM image) of three representative planar acetylene-linked oxa-nanographene dimers (**a**: *α,α*-dimer; **c**: *β,β*-dimer; **e**: *α,β*-dimer). The gray curves were taken on a bare Au(111) surface, demonstrating the Shockley surface state of Au(111) at around −0.4 V. **b, d**, **f** Constant-current dI/dV maps of three representative planar acetylene-linked oxa-nanographene dimers (**b**: *α,α*-dimer; **d**: *β,β*-dimer; **f**: *α,β*-dimer) conducted at indicated energies and the corresponding calculated LDOS of HUMO and mixed LUMO containing LUMO and LUMO + 1 (HSE06 results, see detailed settings in Methods). The Fermi level is set to zero. Scale bars of STM images: 0.5 nm. Scanning parameters of STM images: **a** $U = 0.6$ V, $I = 200$ pA. **c** $U = 0.1$ V, $I = 50$ pA. **e** $U = 0.5$ V, $I = 50$ pA.

https://doi.org/10.1038/s41467-024-53927-6

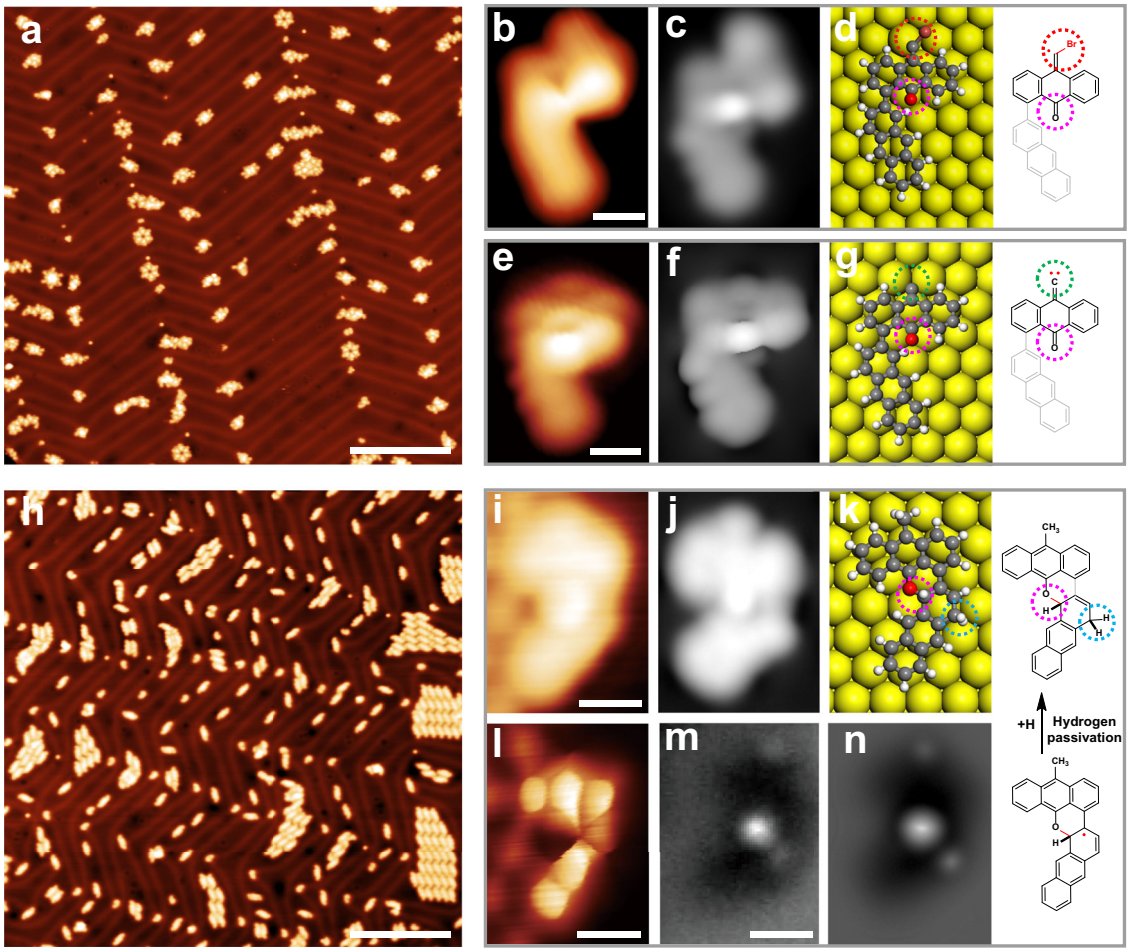

Fig. 4 | Structural characterization of representative nonplanar reaction intermediates on Au(111). a Large-scale STM image after depositing precursor **1** on a cold Au(111). **b, e** Zoom-in and **c**, **f** simulated STM images of two individual debromination intermediates and the corresponding **d, g** structural models and chemical structures. **h** Large-scale STM image after annealing at approximately 300 K for 12 h. **i** Zoom-in STM, **j** simulated STM, **l** BR-STM, **m** nc-AFM, and **n** simulated AFM images of an individual cyclization intermediate I and **k** the corresponding structural model and chemical structure. The gray chemical structure represents the part of the molecule closer to the Au(111) surface. Scale bars: **a, h** 20 nm. **b**, **e**, **i**, **l**, **m** 0.5 nm. Scanning parameters: **a** $U = 1$ V, $I = 10$ pA. **b** $U = 0.01$ V, $I = 10$ pA. **e** $U = 50$ mV, $I = 100$ pA. **h** $U = 0.5$ V, $I = 10$ pA. **i** $U = 0.1$ V, $I = 100$ pA. **l** CO tip, constant height, $U = 10$ mV.

voltages can be assigned as the HOMO and mixed LUMO containing LUMO and LUMO + 1 of the planar oxa-nanographenes, respectively. The experimental HOMO-LUMO gaps of three oxa-nanographenes (approximately 2.1–2.3 V, Fig. 3a, c, e) are similar. In contrast, the calculated HOMO-LUMO gaps of the three free-standing oxa-nanographenes show that the gap for α,α-dimer (1.86 eV, Supplementary Fig. 9a) is slightly larger than those for the β,β-dimer (1.67 eV, Supplementary Fig. 9c) and α,β-dimer (1.67 eV, Supplementary Fig. 9e). These results may be ascribed to the differences in electronic coupling between the molecule and the Au(111) substrate.

To explore the reaction mechanism of room-temperature cyclodehydrogenation on Au(111), we progressively annealed two cold Au(111) samples with different coverage. For a submonolayer of precursor **1** deposited on a cold Au(111) surface, the STM images (Fig. 4a) reveal that most of the species are randomly distributed to form diverse aggregates consisting of nonplanar geometries, and only a few individual monomers can be observed. The zoom-in and constant-height STM images (Supplementary Fig. 10) of the three representative aggregates show that two regular structures are self-assembled hexamer and tetramer, while the irregular structure is a self-assembly of short chains. A careful comparison of the experimental STM images and the simulations based on DFT-optimized structure models (Supplementary Fig. 11) suggests that the hexamer is composed of six intact precursors **1** species with a *trans*-up adsorption geometry (Supplementary Fig. 10a, d), while the tetramer consists of four precursors—two with *cis*-up and two with *trans*-up adsorption geometry (Supplementary Fig. 10b, e). The irregular short chain is composed of multiple precursors with mixed adsorption geometries (Supplementary Fig. 10c, f).

Moreover, the STM images of two individual monomers on Au(111) (Fig. 4b and Supplementary Fig. 12a, b) show a bright protrusion at the middle of the two monomers (pink dotted circles in Supplementary Fig. 12a, b) and one slightly dark spot at the terminal (red dotted circles in Supplementary Fig. 12a, b). A careful comparison of the experimental and calculated results (Fig. 4c, f, and Supplementary Fig. 12a, b) suggests that the bright protrusion originates from carbonyl with an upward adsorption configuration wherein this group is disposed away from the surface, while the slightly dark spot originates from unreacted alkenyl bromide. A surface-bound carbene intermediate with a carbonyl disposed in an upward adsorption configuration was also observed and its STM image (Fig. 4e) is in agreement with the simulation based on the DFT-optimized structure model (Fig. 4f, g, and Supplementary Fig. 12c). These results demonstrate that precursor **1** has undergone debromination to form the surface-bound organometallic intermediates on the cold Au(111) substrate, further suggesting that the debromination involves the transformation from low active dibromomethylene (sp2 C–Br activation) of closed-shell resonance structures to highly active dibromomethyl radical (similar

to sp3 C–Br activation) of open-shell resonance structures (Fig. 1c and Supplementary Fig. 1)[61,70].

When the same sample is annealed at room temperature for 12 h, a behavior similar to that of the previous room-temperature sample is observed (Fig. 4h), except that some new regular molecule islands are assembled from planar dimers with bromine adatoms (Supplementary Fig. 13), which are composed of individually dispersed planar dimer and monomer products. Notably, the same experimental results are also obtained after depositing precursor **1** onto Au(111) held at room temperature followed by direct annealing at 333 K for 15 minutes. These results indicate that the diffusion of surface-bound carbene intermediates is slow at room temperature but significantly enhanced at higher annealing temperatures, and thus, the same covalent reaction requires a longer time at room temperature and a shorter time at higher annealing temperatures.

Interestingly, the large-scale STM images reveal two kinds of unique species corresponding to a slightly brighter region (Fig. 4i and Supplementary Fig. 15). The zoom-in STM (Fig. 4i), BR-STM (Fig. 4l), and nc-AFM (Fig. 4m and Supplementary Fig. 14) images show that the size of species I is the same as that of the planar monomer, although the slightly brighter feature of the central backbone is different from that of the planar monomer. A careful comparison of the experimental results (Fig. 4i, l, and m) and simulations based on the DFT-optimized structure models (Fig. 4j, k, n) suggests that species I is a nonplanar intermediate derived from the hydrogen passivation of the intramolecular radical addition intermediate[20]. Moreover, the zoom-in STM, BR-STM and nc-AFM images of species II (Supplementary Fig. 15) reveal a similar geometry as that of the planar dimer, while the upper half of the molecular skeleton is the same as that of the planar monomer, and the lower half is similar to that of species I. These features further demonstrate that cyclodehydrogenation involves intramolecular radical addition. Notably, various other nonplanar species were also observed, including monomers with a slightly dark region and dimers with two slightly brighter regions (Supplementary Figs. 16 and 17). However, because of the unique nonplanar features, their accurate chemical structures were still not determined by STM, BR-STM, and nc-AFM imaging and DFT calculations. The further experimental results show that as the room temperature annealing time increases, the nonplanar species gradually decrease until they disappear, suggesting that the non-planar species are intermediates of forming desired planar products.

When another cold Au(111) sample with high coverage precursor **1** was annealed at room temperature for 2 h, only a few planar dimer products were formed and most species were debrominated carbene intermediates stabilized by the Au(111) surface (Supplementary Fig. 18a). After annealing at room temperature for 6 h, the abundance of the planar dimer products increases significantly (Supplementary Fig. 18b). Further annealing at room temperature for 12 h reveal the formation of large-scale regular molecule islands are assembled from planar dimers with bromine adatoms (Supplementary Fig. 18c). These results suggest that molecular coverage does not significantly affect diffusion of surface-bound carbene intermediates and subsequent C-C coupling as well as room-temperature cyclodehydrogenation.

To elucidate the mechanism of highly chemoselective room-temperature cyclodehydrogenation on Au(111), we performed the corresponding DFT calculations (Fig. 5). In the direct debromination of precursor **1** with the most stable *cis*-up adsorption geometry on Au(111) to form the surface-bound debromination intermediate (*cis*-Int3), the calculated reaction barrier is 0.96 eV (Supplementary Fig. 19). In comparison, the highest reaction barrier in the indirect debromination process, including the transformation of the adsorption geometry from a *cis*-up to *cis*-down configuration (0.65 eV, energy levels from *cis*-IS1 to *cis*-Int1 in Fig. 5a), debromination (0.69 eV, energy levels from *cis*-Int1 to *cis*-Int2 in Fig. 5a), and transformation of the adsorption geometry from a *cis*-down to *cis*-up configuration (0.32 eV, energy levels from *cis*-Int2 to *cis*-Int3 in Fig. 5a), is 0.27 eV lower than that of the direct debromination of precursor **1** with a *cis*-up adsorption geometry. Moreover, the reaction barrier for the second debromination from *cis*-Int3 to *cis*-Int4 is only 0.58 eV. Notably, the debromination intermediate (*cis*-Int2) to carbene intermediate (*cis*-Int4) may also be via the second debromination followed by transformation of the adsorption geometry (Supplementary Fig. 20), in which the highest energy barrier (0.61 eV) is 0.08 eV lower than that of the first indirect debromination. These results demonstrate that the indirect debromination pathways to form carbene intermediates (*cis*-Int4) are energetically favorable.

The highest reaction barrier for the indirect debromination pathway of precursor **1** with *trans*-up adsorption geometry is 0.79 eV (Supplementary Fig. 21), which is only 0.1 eV greater than that of precursor **1** with *cis*-up adsorption geometry. In addition, the calculated barrier of the C–C coupling of carbene intermediates (approximately 0.8 eV, Supplementary Fig. 22) is also similar to that of the highest reaction barrier of the indirect debromination step, while the reaction energy of this exothermic step is approximately 3.2 eV, reflecting the irreversibility of the C–C bond formation. These results suggest that the high chemoselectivity of cyclodehydrogenation does not originate from the differences in the debromination and C–C coupling steps of precursor **1** caused by the adsorption geometry.

The final intramolecular cyclodehydrogenation step includes the addition of O-radicals to the adjacent phenyl group and the hydrogen elimination (Fig. 5b, c), which utilizes two simplified radical intermediates (*cis*-IS3 and *trans*-IS3). The calculated reaction barriers for the two possible radical addition pathways are similar and essentially the same as the highest reaction barrier of the indirect debromination step. Notably, DFT calculations show that the two possible radical addition pathways are endothermic processes, wherein intermediate *cis*-Int6 is more stable than *trans*-Int6. This result suggests that *trans*-Int6 undergoes a reversible reaction more readily to recover *trans*-IS3, which may further form *cis*-IS3 through the transformation of the adsorption geometry. In addition, hydrogen elimination is a spontaneous exothermic aromatization process, excluding the possibility that the difference in α- or β-H elimination controls the chemoselectivity of cyclodehydrogenation. Therefore, the high chemoselectivity of cyclodehydrogenation can be attributed to the reversibility and different thermodynamics of the radical addition step.

Based on the geometric structures and configurations of the experimentally observed products and intermediates and DFT calculations, a plausible mechanism involving stepwise debromination, C–C coupling, and radical addition/dehydrogenation to form planar acetylene-linked oxa-nanographenes with high chemoselectivity on Au(111) was proposed (Supplementary Fig. 23). Precursors **1** or its open-shell resonance structure first undergo stepwise debromination to form surface-bound carbene intermediates. Subsequently, the C–C coupling of carbenes gives the nonplanar dimer intermediates. Finally, intramolecular radical addition generates nonplanar cyclized intermediates, that easily undergo dehydrogenation to attain planarization and aromatization, affording the desired acetylene-linked oxa-nanographenes.

To further demonstrate the generality of the radical addition of open-shell resonance structures in the on-surface synthesis of molecular structures, we performed the same experiments on the Ag(111) substrate. As shown in the Supplementary Fig. 24, an irregular molecular island was formed after depositing precursor **1** on the Ag(111) surface held at room temperature for 24 h under UHV conditions (Supplementary Fig. 24a). High-resolution STM image shows that the irregular molecular islands are mainly composed of a small amount of monomers, a large amount of non-planar and planar dimer products, and bromine atoms, indicating that at room temperature some molecules on Ag(111) undergo a debromination C–C coupling and cyclodehydrogenation cascade reaction similar to that on Au(111). It is noteworthy that the slight difference in the reactivity of the two

https://doi.org/10.1038/s41467-024-53927-6

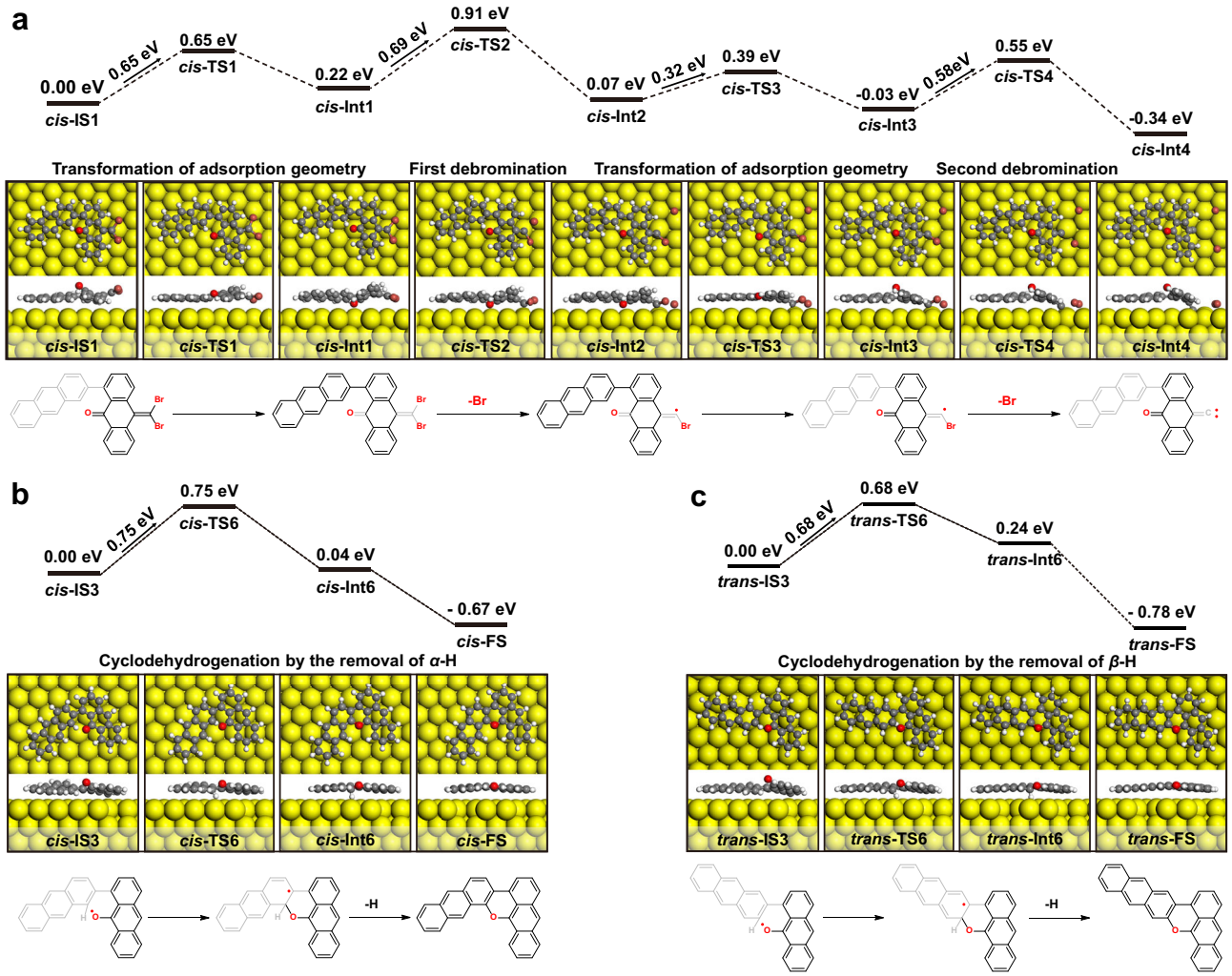

Fig. 5 | Reaction pathway of room-temperature debromination and cyclodehydrogenation on Au(111). a The transformation of adsorption geometry and debromination to form surface-bound carbene intermediates. **b**, **c** Cyclodehydrogenation by the removal of α- or β-H. The corresponding calculated molecular structures including top and side views of the initial (IS), transition (TS), and intermediate (Int) states of the reactions are shown below the energy diagrams (CI-NEB method, see detailed settings in Methods). The reaction pathways of chemical structures are shown below the molecular structure models (The gray chemical structure represents the part of the molecule closer to the Au(111) surface).

substrates at room temperature may be due to the different interactions between the reaction intermediates and the metal substrate. When the same sample was further annealed at 333 K for 15 min, large-scale regular phases were formed and composed of planar dimers and Br atoms (Supplementary Fig. 24b). High-resolution STM and BR-STM images further confirmed the chemical structure of planar dimer products (Supplementary Fig. 24c). These results demonstrate that the radical addition of the open-shell resonance structures in molecules on Ag(111) is also effective in lowering the reaction temperature of intramolecular cyclodehydrogenation.

Discussion

In summary, we developed a room-temperature cyclodehydrogenation on Au(111) via radical addition of open-shell resonance structures and demonstrated that radical addition significantly lowered the temperature of cyclodehydrogenation and further improved the chemoselectivity of dehydrogenation. Various planar acetylene-linked oxa-nanographenes were synthesized from a nonplanar precursor on Au(111). The chemical structures of the oxa-nanographenes and the diverse nonplanar intermediates were determined by a combination of high-resolution STM, BR-STM, and nc-AFM. STS measurements revealed the molecular orbitals of oxa-nanographenes on Au(111), whose HOMO and LUMO distributions were determined using the dI/dV maps and verified using DFT calculations. The nonplanar intermediates observed during progression annealing demonstrated that the formation of the planar acetylene-linked oxa-nanographenes involved stepwise debromination to form surface-bound carbenes, C–C coupling of carbenes, and intramolecular radical addition/hydrogen elimination to attain planarization and aromatization. In addition, DFT calculations suggest that the high chemoselectivity of the cyclodehydrogenation results from the reversibility and different thermodynamics of the radical addition step. Our findings provide new insights for realizing low-temperature dehydrogenation reactions and hence improving the selectivity of on-surface reactions, which are crucial in the controllable fabrication of planar carbon-based nanomaterials. Furthermore, the radical addition of open-shell resonance structures may be applied in developing insulating surface covalent coupling reactions, thereby enabling the direct synthesis and intrinsic properties exploration of molecules on insulating surfaces.

Methods

Sample preparation and STM/AFM measurements

Single crystalline Au(111) surface was cleaned by cycles of Ar^+ sputtering and annealing under UHV (base pressure 2×10^{-10} mbar).

Precursor **1** was evaporated from a quartz crucible onto the Au(111) surface held at the indicated temperatures, and the sublimation temperature was approximately 150 °C. Then, the progression annealing at evaluated temperatures and times was performed. The preparation process of the two cold Au(111) samples is as follows: first, the Au(111) substrate is precooled to 5 K; second, the cold Au(111) is quickly transferred to the sample stage maintained at 293 K, and the precursor **1** is deposited on the cold Au(111) surface; finally, the cold Au(111) sample is quickly transferred to the sample stage maintained at 5 K (the whole process takes less than 3 min). STM measurements were performed on a Scienta Omicron POLAR-STM/AFM combined system operated at approximately 5 or 77 K with an electrochemically etched tungsten tip. The STM images were taken in the constant-current mode using a tungsten tip and the voltages refer to the bias on samples concerning the tip. The bond-resolved STM images were acquired with a low-temperature STM (Scienta Omicron POLAR-STM/AFM combined system) operated at approximately 5 K. The qplus tip was modified with a single CO molecule at the tip apex. AFM measurements were performed in non-contact mode with a qPlus sensor at 5 K. The sensor was operated in frequency modulation mode with a constant oscillation amplitude of 0.3 Å. AFM measurements were performed in constant-height mode with $U = 2$ mV. The dI/dV spectra were obtained with a lock-in amplifier, while the sample bias was modulated by a 511 Hz, 20 mV sinusoidal signal under open-feedback conditions. The dI/dV maps were acquired in constant-current mode.

Theoretical calculations

The calculations were carried out in the framework of DFT by using the Vienna ab initio Simulation Package (VASP)[71]. The projector augmented-wave (PAW) method described the interaction between ions and electrons[72]. We used the generalized gradient approximation (GGA) with Perdew-Burke-Ernzerhof (PBE) formalism to treat exchange-correlation interaction[73], and van der Waals (vdW) interactions were considered by using the DFT-D3 developed by Grimme[74]. The energy cutoff for the plane wave basis sets is 400 eV, and the energy and force convergence value between two consecutive self-consistent steps were set as 10^{-6} eV and 0.05 eV/Å, respectively. The simulations of the reaction barriers in the manuscript (Fig. 5 and Supplementary Figs. 19-22) are performed with the climbing image nudged elastic band (CI-NEB) method for finding saddle points and minimum energy paths (http://theory.cm.utexas.edu/vtsttools/neb.html), which is at T = 0 without including entropy and vibrations[75]. The STM simulations in Fiure 4 and Supplementary Figs. 11 and 12 were performed with the Tersoff-Hamman method[76]. Besides, we calculated the electronic properties of planar acetylene-linked oxa-nanographenes (in Fig. 3 and Supplementary Fig. 9) using the hybrid functional HSE06[77] in the gas phase. The Brillouin zone (BZ) was sampled in the Gamma centered Monkhorst-Pack grids with a $2 \times 1 \times 1$ *k*-point sampling and a Gaussian smearing with an energy width of 0.05 eV.

Data availability

The authors declare that the main data supporting the findings of this study are available within the paper and its Supplementary Information files. Extra data are available from the corresponding authors upon request. Source data are provided with this paper (see the data https://doi.org/10.6084/m9.figshare.27202401).

References

1. Fu, P. P. & Harvey, R. G. Dehydrogenation of polycyclic hydroaromatic compounds. *Chem. Rev.* **78**, 317–361 (1978).
2. Grant, J. T., Venegas, J. M., McDermott, W. P. & Hermans, I. Aerobic Oxidations of Light Alkanes over Solid Metal Oxide Catalysts. *Chem. Rev.* **118**, 2769–2815 (2018).
3. Docherty, S. R., Rochlitz, L., Payard, P.-A. & Copéret, C. Heterogeneous Alkane Dehydrogenation Catalysts Investigated *via* a Surface Organometallic Chemistry Approach. *Chem. Soc. Rev.* **50**, 5806–5822 (2021).
4. Zhang, Y., Pun, S. H. & Miao, Q. The Scholl Reaction as a Powerful Tool for Synthesis of Curved Polycyclic Aromatics. *Chem. Rev.* **122**, 14554–14593 (2022).
5. Zhong, D. et al. Linear Alkane Polymerization on a Gold Surface. *Science* **334**, 213–216 (2011).
6. Li, X. et al. Direct Transformation of *n* -Alkane into All- *Trans* Conjugated Polyene via Cascade Dehydrogenation. *Nat. Sci. Rev.* **8**, nwab093 (2021).
7. Mallada, B. et al. On-Surface Strain-Driven Synthesis of Non-alternant Non-Benzenoid Aromatic Compounds Containing Four- to Eight-Membered Rings. *J. Am. Chem. Soc.* **143**, 14694–14702 (2021).
8. Liu, L. et al. Polymerization of Silanes through Dehydrogenative Si–Si Bond Formation on Metal Surfaces. *Nat. Chem.* **13**, 350–357 (2021).
9. Kinikar, A. et al. On-Surface Polyarylene Synthesis by Cycloaromatization of Isopropyl Substituents. *Nat. Synth.* **1**, 289–296 (2022).
10. Gao, Y. et al. Selective Activation of Four Quasi-Equivalent C–H Bonds Yields N-Doped Graphene Nanoribbons with Partial Corannulene Motifs. *Nat. Commun.* **13**, 6146 (2022).
11. Zhang, Y.-Q. et al. Synthesizing Highly Regular Single-Layer Alkynyl–Silver Networks at the Micrometer Scale via Gas-Mediated Surface Reaction. *J. Am. Chem. Soc.* **141**, 5087–5091 (2019).
12. Sánchez-Sánchez, C. et al. On-Surface Hydrogen-Induced Covalent Coupling of Polycyclic Aromatic Hydrocarbons via a Superhydrogenated Intermediate. *J. Am. Chem. Soc.* **141**, 3550–3557 (2019).
13. Zhang, C., Kazuma, E. & Kim, Y. Steering the Reaction Pathways of Terminal Alkynes by Introducing Oxygen Species: From C–C Coupling to C–H Activation. *J. Am. Chem. Soc.* **144**, 10282–10290 (2022).
14. Lowe, B. et al. Selective Activation of Aromatic C–H Bonds Catalyzed by Single Gold Atoms at Room Temperature. *J. Am. Chem. Soc.* **144**, 21389–21397 (2022).
15. Björk, J. et al. The Role of Metal Adatoms in a Surface-Assisted Cyclodehydrogenation Reaction on a Gold Surface. *Angew. Chem. Int. Ed.* **61**, e202212354 (2022).
16. Li, Q. et al. Hierarchical Dehydrogenation Reactions on a Copper Surface. *J. Am. Chem. Soc.* **140**, 6076–6082 (2018).
17. Sun, K. et al. Surface-Assisted Alkane Polymerization: Investigation on Structure–Reactivity Relationship. *J. Am. Chem. Soc.* **140**, 4820–4825 (2018).
18. Treier, M. et al. Surface-Assisted Cyclodehydrogenation Provides a Synthetic Route towards Easily Processable and Chemically Tailored Nanographenes. *Nat. Chem.* **3**, 61–67 (2011).
19. Ma, C. et al. On-Surface Cyclodehydrogenation Reaction Pathway Determined by Selective Molecular Deuterations. *Chem. Sci.* **12**, 15637–15644 (2021).
20. Zhong, Q. et al. A. Deciphering the Mechanism of On-Surface Dehydrogenative C–C Coupling Reactions. *J. Am. Chem. Soc.* **146**, 1849–1859 (2024).
21. Talirz, L., Ruffieux, P. & Fasel, R. On-Surface Synthesis of Atomically Precise Graphene Nanoribbons. *Adv. Mater.* **28**, 6222–6231 (2016).
22. Sun, Q., Zhang, R., Qiu, J., Liu, R. & Xu, W. On-Surface Synthesis of Carbon Nanostructures. *Adv. Mater.* **30**, 1705630 (2018).
23. Clair, S. & de Oteyza, D. G. Controlling a Chemical Coupling Reaction on a Surface: Tools and Strategies for On-Surface Synthesis. *Chem. Rev.* **119**, 4717–4776 (2019).
24. Grill, L. & Hecht, S. Covalent On-Surface Polymerization. *Nat. Chem.* **12**, 115–130 (2020).

25. Chen, Z., Narita, A. & Müllen, K. Graphene Nanoribbons: On-Surface Synthesis and Integration into Electronic Devices. *Adv. Mater.* **32**, 2001893 (2020).
26. Jolly, A., Miao, D., Daigle, M. & Morin, J. Emerging Bottom-Up Strategies for the Synthesis of Graphene Nanoribbons and Related Structures. *Angew. Chem. Int. Ed.* **59**, 4624–4633 (2020).
27. Su, J., Telychko, M., Song, S. & Lu, J. Triangulenes: From Precursor Design to On-Surface Synthesis and Characterization. *Angew. Chem. Int. Ed.* **59**, 7658–7668 (2020).
28. Song, S. et al. On-Surface Synthesis of Graphene Nanostructures with π-Magnetism. *Chem. Soc. Rev.* **50**, 3238–3262 (2021).
29. Yin, R., Wang, Z., Tan, S., Ma, C. & Wang, B. On-Surface Synthesis of Graphene Nanoribbons with Atomically Precise Structural Heterogeneities and On-Site Characterizations. *ACS Nano* **17**, 17610–17623 (2023).
30. Su, J., Lyu, P. & Lu, J. Atomically Precise Imprinting π-Magnetism in Nanographenes via Probe Chemistry. *Precis. Chem.* **1**, 565–575 (2023).
31. Zhong, Q. et al. Benzo-Fused Periacenes or Double Helicenes? Different Cyclodehydrogenation Pathways on Surface and in Solution. *J. Am. Chem. Soc.* **141**, 7399–7406 (2019).
32. Mishra, S. et al. Synthesis and Characterization of π-Extended Triangulene. *J. Am. Chem. Soc.* **141**, 10621–10625 (2019).
33. Fan, Q. et al. On-Surface Synthesis and Characterization of a Cycloarene: C108 Graphene Ring. *J. Am. Chem. Soc.* **142**, 894–899 (2020).
34. Mishra, S. et al. Large Magnetic Exchange Coupling in Rhombus-Shaped Nanographenes with Zigzag Periphery. *Nat. Chem.* **13**, 581–586 (2021).
35. Xiang, F. et al. Planar π-Extended Cycloparaphenylenes Featuring an All-Armchair Edge Topology. *Nat. Chem.* **14**, 871–876 (2022).
36. Lawrence, J. et al. Topological Design and Synthesis of High-Spin Aza-Triangulenes without Jahn–Teller Distortions. *ACS Nano* **17**, 20237–20245 (2023).
37. Cai, J. et al. Atomically Precise Bottom-up Fabrication of Graphene Nanoribbons. *Nature* **466**, 470–473 (2010).
38. Ruffieux, P. et al. On-Surface Synthesis of Graphene Nanoribbons with Zigzag Edge Topology. *Nature* **531**, 489–492 (2016).
39. Gröning, O. et al. Engineering of Robust Topological Quantum Phases in Graphene Nanoribbons. *Nature* **560**, 209–213 (2018).
40. Rizzo, D. J. et al. Topological Band Engineering of Graphene Nanoribbons. *Nature* **560**, 204–208 (2018).
41. Rizzo, D. J. et al. Inducing Metallicity in Graphene Nanoribbons via Zero-Mode Superlattices. *Science* **369**, 1597–1603 (2020).
42. Blackwell, R. E. et al. Spin Splitting of Dopant Edge State in Magnetic Zigzag Graphene Nanoribbons. *Nature* **600**, 647–652 (2021).
43. Fan, Q. et al. Biphenylene Network: A Nonbenzenoid Carbon Allotrope. *Science* **372**, 852–856 (2021).
44. Pouget, E. et al. Well-Architectured Poly(Dimethylsiloxane)-Containing Copolymers Obtained by Radical Chemistry. *Chem. Rev.* **110**, 1233–1277 (2010).
45. Studer, A. & Curran, D. P. Catalysis of Radical Reactions: A Radical Chemistry Perspective. *Angew. Chem. Int. Ed.* **55**, 58–102 (2016).
46. Wang, X. & Studer, A. Iodine(III) Reagents in Radical Chemistry. *Acc. Chem. Res.* **50**, 1712–1724 (2017).
47. Crespi, S. & Fagnoni, M. Generation of Alkyl Radicals: From the Tyranny of Tin to the Photon Democracy. *Chem. Rev.* **120**, 9790–9833 (2020).
48. Nagib, D. A. Asymmetric Catalysis in Radical Chemistry. *Chem. Rev.* **122**, 15989–15992 (2022).
49. Grill, L. et al. Nano-Architectures by Covalent Assembly of Molecular Building Blocks. *Nat. Nanotechnol.* **2**, 687–691 (2007).
50. Shu, C.-H. et al. On-Surface Synthesis of Poly(p-Phenylene Ethynylene) Molecular Wires via in Situ Formation of Carbon-Carbon Triple Bond. *Nat. Commun.* **9**, 2322 (2018).
51. de Oteyza, D. G. et al. Direct Imaging of Covalent Bond Structure in Single-Molecule Chemical Reactions. *Science* **340**, 1434–1437 (2013).
52. Sun, Q. et al. On-Surface Formation of One-Dimensional Polyphenylene through Bergman Cyclization. *J. Am. Chem. Soc.* **135**, 8448–8451 (2013).
53. Riss, A. et al. Imaging Single-Molecule Reaction Intermediates Stabilized by Surface Dissipation and Entropy. *Nat. Chem.* **8**, 678–683 (2016).
54. Wang, Y. et al. Two-Dimensional Nonbenzenoid Heteroacene Crystals Synthesized via In-Situ Embedding of Ladder Bipyrazinylenes on Au(111). *Angew. Chem. Int. Ed.* **63**, e202318142 (2024).
55. Wang, W. et al. Single-Molecule Resolution of an Organometallic Intermediate in a Surface-Supported Ullmann Coupling Reaction. *J. Am. Chem. Soc.* **133**, 13264–13267 (2011).
56. Björk, J., Hanke, F. & Stafström, S. Mechanisms of Halogen-Based Covalent Self-Assembly on Metal Surfaces. *J. Am. Chem. Soc.* **135**, 5768–5775 (2013).
57. Fritton, M. et al. The Role of Kinetics versus Thermodynamics in Surface-Assisted Ullmann Coupling on Gold and Silver Surfaces. *J. Am. Chem. Soc.* **141**, 4824–4832 (2019).
58. Yu, X. et al. Bond-Scission-Induced Structural Transformation from Cumulene to Diyne Moiety and Formation of Semiconducting Organometallic Polyyne. *J. Am. Chem. Soc.* **142**, 8085–8089 (2022).
59. Zhong, Q. et al. Substrate-Modulated Synthesis of Metal–Organic Hybrids by Tunable Multiple Aryl–Metal Bonds. *J. Am. Chem. Soc.* **144**, 8214–8222 (2022).
60. Stolz, S. et al. Reversible Dehalogenation in On-Surface Aryl–Aryl Coupling. *Angew. Chem. Int. Ed.* **59**, 14106–14110 (2020).
61. Tang, Y. et al. On-Surface Debromination of 2,3-Bis(dibromomethyl)- and 2,3-Bis(bromomethyl)naphthalene: Dimerization or Polymerization? *Angew. Chem. Int. Ed.* **61**, e202204123 (2022).
62. Di Giovannantonio, M. et al. On-Surface Synthesis of Antiaromatic and Open-Shell Indeno[2,1-b]fluorene Polymers and Their Lateral Fusion into Porous Ribbons. *J. Am. Chem. Soc.* **141**, 12346–12354 (2019).
63. Mendieta-Moreno, J. I. et al. Unusual Scaffold Rearrangement in Polyaromatic Hydrocarbons Driven by Concerted Action of Single Gold Atoms on a Gold Surface. *Angew. Chem. Int. Ed.* **61**, e202208010 (2022).
64. Mishra, S. et al. Bistability between π-diradical open-shell and closed-shell states in indeno[1,2-a]fluorene. *Nat. Chem.* **16**, 755–761 (2024).
65. Sánchez-Grande, A. et al. On-Surface Synthesis of Ethynylene-Bridged Anthracene Polymers. *Angew. Chem. Int. Ed.* **58**, 6559–6563 (2019).
66. Cirera, B. et al. Tailoring Topological Order and π-Conjugation to Engineer Quasi-Metallic Polymers. *Nat. Nanotechnol.* **15**, 437–443 (2020).
67. Li, D.-Y. et al. Ladder Phenylenes Synthesized on Au(111) Surface via Selective [2+2] Cycloaddition. *J. Am. Chem. Soc.* **143**, 12955–12960 (2021).
68. Kong, H. et al. Substrate-Mediated C–C and C–H Coupling after Dehalogenation. *J. Am. Chem. Soc.* **139**, 3669–3675 (2017).
69. de la Torre, B. et al. Tailoring π-Conjugation and Vibrational Modes to Steer on-Surface Synthesis of Pentalene-Bridged Ladder Polymers. *Nat. Commun.* **11**, 4567 (2020).
70. Pérez-Elvira, E. et al. Generating antiaromaticity in polycyclic conjugated hydrocarbons by thermally selective skeletal rearrangements at interfaces. *Nat. Synth.* **2**, 1159–1170 (2023).
71. Kresse, G. & Furthmüller, J. Efficient Iterative Schemes for Ab Initio Total-Energy Calculations Using a Plane-Wave Basis Set. *Phys. Rev. B* **54**, 11169–11186 (1996).

72. Blöchl, P. E. Projector Augmented-Wave Method. *Phys Rev B* **50**, 17953–17979 (1994).
73. Perdew, J. P., Burke, K. & Ernzerhof, M. Generalized Gradient Approximation Made Simple. *Phys. Rev. Lett.* **77**, 3865–3868 (1996).
74. Grimme, S. Semiempirical GGA-Type Density Functional Constructed with a Long-Range Dispersion Correction. *J. Comput. Chem.* **27**, 1787–1799 (2006).
75. Henkelman, G. & Jónsson, H. A climbing image nudged elastic band method for finding saddle points and minimum energy paths. *J. Chem. Phys.* **113**, 9901–9904 (2000).
76. Tersoff, J. & Hamann, D. R. Theory and Application for the Scanning Tunneling Microscope. *Phys. Rev. Lett.* **50**, 1998 (1983).
77. Paier, J. et al. Screened hybrid density functionals applied to solids. *J. Chem. Phys.* **124**, 154709 (2006).

Acknowledgements

This work was supported by the National Natural Science Foundation of China (Nos. 22272050, 21925201, 22161160319 and 22302068), the Shanghai Municipal Science and Technology Qi Ming Xing Project (No. 22QA1403000), the Shanghai Sailing Program (23YF1408700), China Postdoctoral Science Foundation (2023M731080), and the Fundamental Research Funds for the Central Universities.

Author contributions

D.-Y.L. and P.-N.L. conceived and supervised the project. Z.-Y.H., J.-H.F., Y.W., G.-Y.X., and Y.Z. performed on-surface synthesis and scanning probe microscopy experiments. D.-Y.L. and L.-X.K. conducted theoretical computations. D.-Y.L. designed the molecules. B.-X.W. and X.-Y.Z. synthesized the molecular precursors. D.-Y.L., Z.-Y.H., and L.-X.K. analyzed the data. D.-Y.L. wrote the manuscript; All authors discussed the results and helped write the manuscript at all stages.

Competing interests

The authors declare no competing interests.

Additional information

Supplementary information The online version contains supplementary material available at https://doi.org/10.1038/s41467-024-53927-6.

Correspondence and requests for materials should be addressed to Deng-Yuan Li or Pei-Nian Liu.

Peer review information *Nature Communications* thanks Xinliang Feng and the other, anonymous, reviewer(s) for their contribution to the peer review of this work. A peer review file is available.